ELSEVIER

Journal of Electron Spectroscopy and Related Phenomena 100 (1999) 237–257

JOURNAL OF ELECTRON SPECTROSCOPY and Related Phenomena

www.elsevier.nl/locate/elspec

Valence and inner shell non-dipole excitation spectroscopy of polyatomic molecules by angle-resolved inelastic electron scattering at high energy

K.T. Leung

Department of Chemistry, University of Waterloo, Waterloo, Ontario N2L 3G1, Canada

Received 13 January 1999; accepted 5 March 1999

Abstract

High energy (>2 keV) electron scattering has been used extensively in the past three decades as an effective method to simulate equivalent photon-impact experiments under dipole-dominated small-angle scattering conditions (the so-called pseudo-photon experiments). More recent studies have focused on its application as a unique spectroscopic tool that provides distinct information about those parts of the electronic structure that are not easily accessible by optical techniques. The capability to excite not just the dipole-allowed transitions but also the dipole-forbidden ones gives electron impact a special advantage for probing electronic excitations and for studying non-dipole phenomena. Indeed, the control of the scattering angle, or equivalently the momentum transfer, provides a powerful means to manipulate electron-induced chemical processes if the excited-state electronic structure can be better understood. This review will give a description of angle-resolved electron energy loss spectroscopy and highlight some of its spectroscopic applications that offer specific information about the electronic structure of the valence and inner shells in polyatomic molecules. Some of the novel aspects of this non-optical technique, including the determination of absolute generalized oscillator strength for non-dipole transitions, will be illustrated by examples drawn from recent studies on CF_3Cl and other related chlorofluorocarbons and hydrochlorofluorocarbons.

Keywords: Angle-resolved electron energy loss spectroscopy; Applications; Valence shells; Inner shells

1. Introduction

The ground-state electronic structure of simple polyatomic molecules has been the subject of intense research both spectroscopically and theoretically. While significant progress in the description of the electronic ground state has been made by using new and improved quantum computational methods, our knowledge about the electronic structure of the excited state is far from complete [1]. It is in principle possible to determine the electronic structure of an excited state by measuring excited-state-related properties, such as the transition energy and oscillator strength of a particular electronic transition, if the ground-state electronic structure is known or well understood. In the past three decades, electron scattering has evolved as a powerful tool for investigating the electronic structure of matter and electron-induced processes. In a typical inelastic electron scattering process, the transfer of energy and

E-mail address: tong@uwaterloo.ca (K.T. Leung)

0368-2048/99/$ – see front matter
PII: S0368-2048(99)00049-3

momentum from the incident electron to the atomic or molecular target can produce both dipole and non-dipole excitations. According to the Bethe theory [2,3], the cross section for a sufficiently fast collision is related to the transition probability, or the so-called generalized oscillator strength (GOS), of the electronic transition of the target from the ground state to an excited state. Comprehensive experimental GOS data (or the so-called Bethe surface) can therefore be used to provide an effective feedback for wavefunction modelling of both the ground and excited states, and for the evaluation and development of new quantum computational methods for the excited states. The importance of GOS for the study of electron-impact phenomena has been reviewed by Inokuti [4].

Angle-resolved electron energy loss spectroscopy (EELS) offers a powerful technique for 'complete' determination of all the excited states, including both the dipole-allowed and the optically inaccessible non-dipole states [5]. The use of angle-resolved EELS for absolute GOS measurement was pioneered by Lassettre et al. [6]. Much of the earlier EELS studies have been devoted to a simulation of photoabsorption and related optical measurements. In particular, Lassettre and coworkers have accurately determined the optical or dipole oscillator strength (DOS) by extrapolating the measured GOS data to the dipole limit [7–9]. Moreover, the so-called pseudo-photon experiments by Brion et al. [10] involve 'near-zero' forward-angle electron scattering at high impact energy, in which the 'distant' collision of the electron effectively simulates the interaction due to a dipole field. One main advantage of these dipole EELS experiments over synchrotron-radiation photoabsorption spectroscopy is the capability of determining absolute cross section data over a wide energy range without performing an 'absolute' measurement [10]. On the other hand, GOS measurements as a function of the scattering angle or, equivalently, the momentum transfer (i.e. away from the dipole limit) provide additional and often unique information about the nature of the electronic transitions and of the electron scattering process itself. In particular, experiments by Bonham et al. [11] and Lassettre et al. [6] have demonstrated the use of these momentum-transfer dependent studies as a powerful means for investigating dipole-forbidden and other multipole excitation phenomena. New non-dipole transitions, which are difficult to detect by using traditional optical methods, have been discovered by using angle-resolved EELS in the valence-shell (including O_2, CO, NO, CO_2, N_2O [12], N_2 [13–17], C_2H_2 [19], benzene [20], and *p*-difluorobenzene [21]) and inner-shell regions (including N 1s in N_2 [22,23] NO and N_2O [23], C 1s in CO [24], CO_2 [25], C_2H_2 [26,27], C_2H_4 and C_6H_6 [27], as well as S 2p [28–30], and S 2s [31] in SF_6).

In this review article, we shall focus on the applications of angle-resolved EELS for the determination of 'unique' electronic structural information and for the study of non-dipole excitation processes. Some of the more prominent concepts will be illustrated with examples drawn from our own studies on 'cage-like' polyatomic molecules, including a series of common chlorofluorocarbons (CFCs), $CF_{4-n}Cl_n$ (n=0–4) [32–35] and their hydrochlorofluorocarbon (HCFC) homologs, $CHF_{3-m}Cl_m$ (m= 1–3) [36–38].

2. Theoretical background

A typical inelastic electron scattering process involves the promotion of an atomic or molecular target from its electronic ground state (M) to an excited state (M*) by transfer of energy and momentum from an incident electron.

$$e^-(E_0,\mathbf{k}_0) + \mathrm{M} \rightarrow e^-(E_0 - E,\mathbf{k}) + \mathrm{M}^* \qquad (1)$$

where E_0 (or $E_0 - E$) and $\mathbf{k}_0$ (or $\mathbf{k}$) are the kinetic energy and momentum of the incident (or scattered) electron, respectively. Fig. 1 shows a schematic

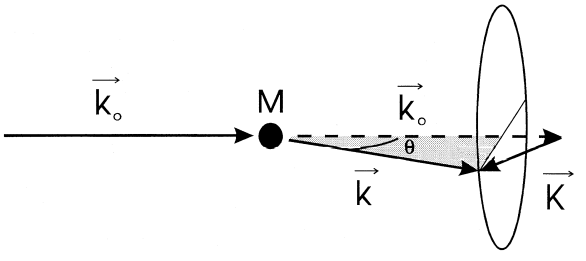

Fig. 1. Schematic diagram of scattering kinematics in a typical electron energy loss process involving non-zero momentum transfer K to a molecular target M.

diagram of the scattering kinematics. The magnitude of the momentum transfer $\mathbf{K}$ ($=\mathbf{k}_0-\mathbf{k}$) is related to the scattering angle θ as follows:

$$K^2 = k_0^2 + k^2 - 2k_0 k\cos\theta. \tag{2}$$

The intensity of the scattered electrons (with the momentum $\mathbf{k}$ and scattering angle θ) that suffer an energy loss E is proportional to the double differential cross section $\frac{d^2\sigma}{d\Omega dE}$. In the first Born approximation, the differential generalized oscillator strength, $\frac{df(K,E)}{dE}$, is related to the cross section by the Bethe–Born formula [4,11]:

$$\frac{df(K,E)}{dE} = \frac{k_0}{k}K^2\frac{E}{4}\frac{d^2\sigma}{d\Omega dE} \tag{3}$$

where $d\Omega$ corresponds to the detection solid angle. All the equations discussed in this section are in Rydberg atomic units. The GOS, $f(K,E)$, is defined as:

$$f(K,E) = \frac{E}{K^2}\left|\left\langle \Psi_n \left| \sum_{j=1}^{N} \exp(i\mathbf{K}\cdot\mathbf{r}_j) \right| \Psi_0 \right\rangle\right|^2, \tag{4}$$

where Ψ_0 and Ψ_n are the N-electron electronic wavefunctions of the initial (ground) and final states, respectively, and $\mathbf{r}_j$ is the position of the jth electron with respect to the centre-of-mass of the target. At small K, the GOS can be expanded into a power series [6,39]:

$$\begin{aligned} f(K,E) &\approx \varepsilon_1^2 + (\varepsilon_2^2 - 2\varepsilon_1\varepsilon_3)|\mathbf{K}|^2 \\ &\quad + (\varepsilon_3^2 - 2\varepsilon_2\varepsilon_4 + 2\varepsilon_1\varepsilon_5)|\mathbf{K}|^4 + \cdots \\ &= f_0 + f_1|\mathbf{K}|^2 + f_2|\mathbf{K}|^4 + \cdots, \end{aligned} \tag{5}$$

where the multipole transition moment is given by

$$\varepsilon_m = \frac{1}{m!}\left\langle \Psi_n \left| \sum_{j=1}^{N} \left(\frac{\mathbf{K}}{|\mathbf{K}|}\cdot\mathbf{r}_j\right)^m \right| \Psi_0 \right\rangle.$$

The GOS therefore converges to the dipole oscillator strength f_0 as the momentum transfer approaches zero [7–9]. If the GOSs at different K values are determined under such conditions that they are relatively normalized to one another, they can be made absolute by single-point normalization at 'zero' momentum transfer to the absolute DOS value obtained by optical techniques (if such data is available). Furthermore, the f_1 term contains information related to the quadrupole transition probability. Studies of the angular dependence of the GOS of a bound state therefore offer a means of obtaining information about the qualitative nature of the transition itself. This is particularly useful for observing dipole-forbidden transitions and for characterizing non-dipole phenomena. For angle-dependent studies that involve finite K values, Lassettre and coworkers [7–9] pointed out that the GOS for a bound-state excitation can be expanded as an even power series of momentum transfer (the so-called Lassettre series):

$$f(K,E) = \frac{1}{(1+x)^6}\sum_{n=0}^{m} f_n\left(\frac{x}{1+x}\right)^n \tag{6}$$

where $x = K^2/[(2I)^{1/2} + (2|I-W|)^{1/2}]^2$, and I is the ionization potential and W is the excitation energy of the discrete transition. The integer m can be chosen according to the available experimental range of momentum transfer [28]. Finally, the GOS for any constant value of K can also be made absolute independently using the Bethe sum rule [4]:

$$\int \frac{df(K,E)}{dE} dE = N, \tag{7}$$

where N is the total number of electrons in the target. With the appropriate fitting procedure that takes account of the background function and the contribution from the other shells [18], the sum-rule normalization procedure provides a convenient means of obtaining absolute cross section without performing an 'absolute' experiment. Since the relative normalization among all the spectra can be maintained automatically by collecting the EELS spectra at different θ angles sequentially in repetitive scans, it is only necessary to perform the sum-rule normalization at a single K value (usually the smallest experimentally accessible K value) to put the entire GOS data on an absolute scale.

Angle-resolved EELS therefore offers an effective technique for 'complete' determination of all the existing excited states, including both the dipole-allowed and the optically inaccessible forbidden or non-dipole transitions. Furthermore, the GOSs measured at different momentum transfer values are related qualitatively to the corresponding Fourier

transform components of the overlap function between the initial-state and final-state wavefunctions (Eq. (4)). In effect, GOS measurement can provide a detailed 'mapping' of the overlap function in momentum space, which can in turn be used as an effective feedback for theoretical modelling of the excited-state wavefunction.

3. Experimental method

The coplanar electron scattering spectrometer used to obtain the intensity of scattered electrons as a function of the energy loss and scattering angle (the EELS spectrum) has been described in detail elsewhere [40]. Briefly, electrons thermionically emitted from a heated hairpin filament were collimated and accelerated to an impact energy of 2.5 keV. The high energy incident electron beam was then crossed with a gas jet expanded from a nozzle (0.5 mm diameter) positioned at 1 cm above the collision centre. Electrons scattered with an energy loss E at an angle θ from the forward direction were analyzed by a hemispherical energy analyser equipped with a seven-element lens. The momentum transfer K is related to the scattering angle θ by Eq. (2). It is important to note that even though our EELS spectra were collected at fixed scattering angles and not at fixed momentum transfers, the change in the momentum transfer with the energy loss can be minimized by using a sufficiently high impact energy. Within the range of $0.5^\circ < \theta < 10^\circ$ employed for the experiments discussed below, the corresponding momentum transfer is effectively constant at 2.5 keV impact energy over the experimental energy loss ranges of interest (e.g. 150 eV in the case of the valence shell, and 50 eV for the C 1s and Cl 2p shells). Our spectrometer is capable of an overall energy resolution of 0.8 eV full-width-at-half-maximum (FWHM) and an angular resolution of 0.5° half-angle. The angular scale was calibrated periodically by comparing the measured GOS of the pre-ionization bound (1s→2p and 1s→2s) transitions of He with reliable theoretical calculations, while the energy loss scale could be calibrated in situ with the energy loss spectrum of a known background gas (such as N_2) [40]. To determine the absolute GOS profiles of the valence-shell transitions, a number of EELS spectra were collected at a series of θ angles (corresponding to different momentum transfer values) sequentially in repetitive scans. The spectral cross sections in these EELS spectra were therefore relatively normalized to one another, and can be converted to relative GOS using the Bethe–Born formula (Eq. (3)). The relative GOS data can be put on an absolute scale using either the Bethe-sum-rule normalization (Eq. (7)) or, if applicable, single-point normalization to any existing absolute optical data in the literature [40].

While the data analysis for valence-shell transitions is relatively straightforward, several notes of caution should be mentioned in the case of inner-shell transitions. First, it should be noted that the momentum transfer value for zero scattering angle, though generally small, could be quite different from zero due to the large energy loss involved for inner-shell transitions. 'True' optical (DOS) data therefore cannot really be obtained even for the dipole EELS experiments performed at 'zero' scattering angle under dipole-dominated (i.e. high impact energy) scattering conditions. Although it is possible to lower the minimal accessible K value by using a smaller impact energy, this may lead to complications in the interpretation of the data due to non-Born effects [29,30]. Since it is possible, though unlikely for inner-shell transitions, that dramatic variations in the GOSs could occur very close to the K origin, the fitted curves representing the Lassettre series expansion (Eq. (6)) may not always be reliable for extracting the DOS values due to the lack of data points below the finite minimal accessible K value (e.g. $K \approx 0.6$ a.u. for C 1s transitions at 2.5 keV impact energy). Given the limited energy loss range of our inner-shell data, it was more straightforward to perform single-point normalization of our near-zero EELS spectrum to the available literature dipole EELS data at an appropriately chosen energy point. Such a single-point normalization between the 'dipole' EELS data and the photoabsorption data has been found to introduce an uncertainty of ~20%. It should be noted that more elaborate normalization procedures could be used, apparently with good results [29,30]. Second, the choice of the mathematical function used to simulate the background could, in many cases, be important particularly for regions where possible weak transitions may occur. Further-

more, the range of the available data set (i.e. over a sufficiently large energy loss range) could have direct consequence on the quality of the fit in approximating the background and its subsequent removal procedures. These important issues of data reduction and the associated errors have been discussed in detail by Barbieri and Bonham [18] and more recently by Hitchcock and coworkers [29,30]. Finally, while detailed intensity calibration as a function of the scattering angle due to such effects as changes in the effective interaction volume between the electron trajectory and the gas jet, etc. is useful, these correction procedures should be checked internally in a self-consistent manner. Careful calibration by using the GOS profile of the He I transition as indicated above is therefore essential to prevent overcorrecting these kinematical effects.

The valence-shell electronic structure of N_2 has been studied extensively by a variety of techniques, including photoabsorption [41–43], dipole EELS [44] and angle-resolved EELS [13–18]. The valence-shell absolute DOS data obtained from these experiments [41–44] are in reasonable agreement with one another and therefore provide an excellent standard for energy (and intensity) calibration purposes. Dipole-forbidden transitions have also been studied in the valence region of N_2 by angle-resolved EELS. In particular, the quadrupole-allowed Lyman–Birge–Hopfield (LBH) band at 9.3 eV represents one of the 'classic' benchmark molecular systems for absolute GOS measurements today. It has not only been determined to a high accuracy at a wide range of impact energy by several experimental groups [13–18], but also been extensively investigated theoretically [45–47]. As a demonstration of the typical performance of our spectrometer, we compare our GOS measurement of the LBH band with the earlier measurements [13–18]. Clearly, Fig. 2 shows that all

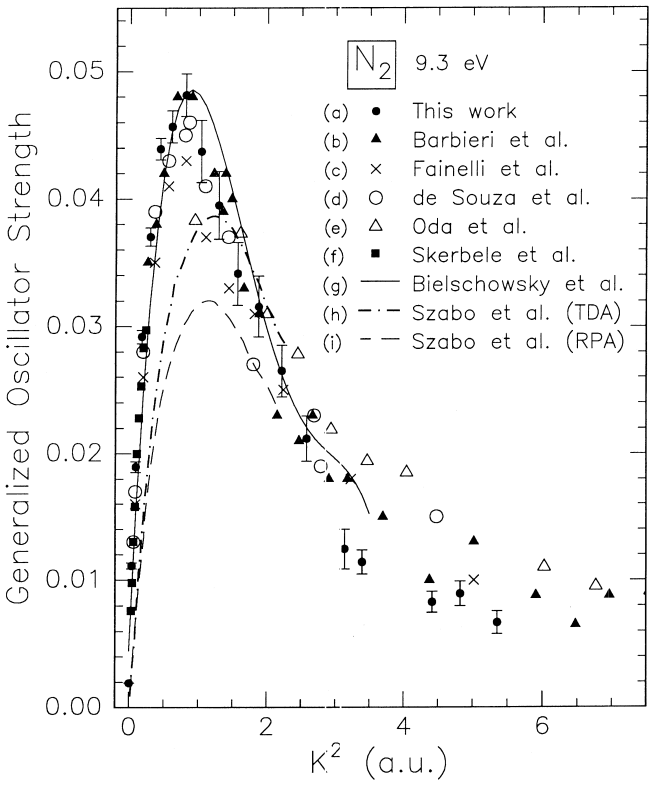

Fig. 2. Comparison of generalized oscillator strength (GOS) profile of the Lyman–Birge–Hopfield band of N_2 with the experimental GOS profiles obtained at different impact energies [13–18] and with calculated profiles [45–47]. The GOS data were made absolute by single-point normalization at $K^2=0.80$ a.u. to the maximum ($f=0.048$) of the data reported by Barbieri and Bonham [18].

the GOS measurements are in good agreement with one another regardless of the very different impact energies (0.3–25 keV). The consistency of the GOS data with respect to the impact energy therefore confirms the validity of the first Born approximation at the presently employed impact energy of 2.5 keV [40]. The theoretical calculations based on the RPA and TDA approximations [45–47] appear to reproduce the general shape of the experimental data correctly. However, only the configuration interaction (CI) calculations are in quantitative agreement with the experiment between $K^2 \approx 0$ and 3 a.u., which suggests the importance of electron correlation effects in GOS calculations [45–47]. Finally, the excellent agreement between our measurement and the earlier experimental and calculated results for this well studied LBH band also demonstrates the reliability of the GOS data obtained by using our spectrometer [40].

4. Application to excited-state spectroscopy of CFC and their substitutes in the valence shell

The study of CFC or freon molecules has continued to be of considerable interest because of their important roles in various atmospheric chemical reactions [48] and plasma etching processes commonly used in the semiconductor industry [49]. These important environmental and industrial applications require an adequate knowledge of the underlying electronic transitions and of their absorption oscillator strengths. CFC and their related halogen-substituted methanes are also of fundamental interest as 'simple' tetrahedron-like or cage-like systems for studying halogen substitutional effects and reactivities of halogen-containing organic molecules. Despite the information on the underlying electronic states provided by photoabsorption spectroscopy and dipole EELS, electronic states that are inaccessible from the ground state by the dipole selection rule will remain difficult to detect using these methods. Using angle-resolved EELS, we have determined the Bethe surfaces of the valence shells of a series of CFCs, $CF_{4-n}Cl_n$ ($n=0$–4) [32–34], and their HCFC homologs, $CHF_{3-m}Cl_m$ ($m=1$–3) [36–38], in the valence-shell (5–150 eV) region. As an example, we show in Fig. 3 the variation of the GOS of the valence-shell energy loss features over an extended momentum transfer range in the form of a Bethe surface plot for CF_3Cl (Freon 13), CF_2Cl_2 (Freon 12) and $CFCl_3$ (Freon 11) [33]. The Bethe surface gives a comprehensive description of the electron–molecule inelastic scattering process, and is particularly useful for analyzing such quantities as the stopping power, total inelastic scattering cross section and polarizability [4]. In particular, Fig. 3a, c and e emphasize the impact-scattering domain of large momentum transfer and energy loss, which corresponds to the kinematical region for 'close' collisions. In this domain, a broad ridge is seen to disperse to a higher energy loss with increasing momentum transfer. This ridge is the result of momentum conservation in the inelastic electron–molecule collision and becomes the well known Bethe ridge in the Born approximation [4]. Fig. 3b, d and f, on the other hand, emphasize the dipole-scattering domain of small momentum transfer and energy loss, which involves 'distant' collisions and where sharp 'optical' features of the valence shell are more apparent. Although the overall appearance of the Bethe surfaces of the three molecules appears to be similar (Fig. 3), the GOS evidently becomes more concentrated in the dipole-scattering region with increasing chlorine content in the CF_3Cl, CF_2Cl_2, and $CFCl_3$ series [33]. This trend can be qualitatively understood by considering the differences in the spatial distributions of the valence-shell electron densities of these molecules. In general, the electron binding energy is inversely related to the size of an orbital (as approximated, e.g., by the average Bohr radius). In the series of CF_3Cl, CF_2Cl_2, and $CFCl_3$ [33], the valence orbitals become more diffuse with successive chlorination, which therefore gives rise to increasingly lower ionization potentials of the valence shell and hence a higher concentration of the GOS in the low energy loss region, as observed in Fig. 3b, d and f. Furthermore, a larger size of the valence shell (as the result of an increased chlorine content) also gives rise to a lower average charge density, hence favouring 'distant' collisions (i.e. those characterized by a small momentum transfer). Consequently, the Bethe surface of $CFCl_3$ appears to be the most strongly peaked in the lower momentum transfer region among the three molecules, giving

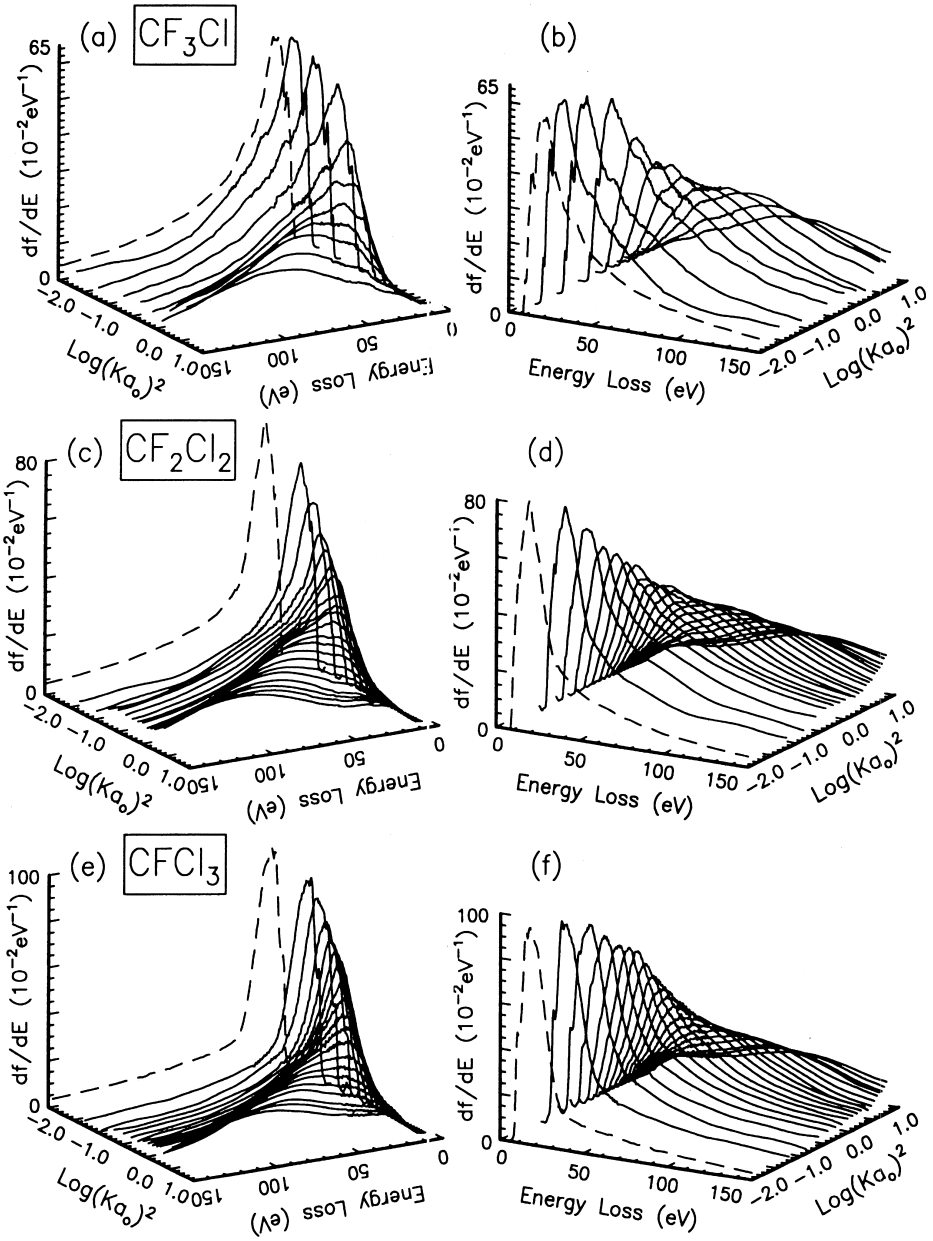

Fig. 3. Bethe surfaces of the valence shells of CF_3Cl (a, b), CF_2Cl_2 (c, d), and $CFCl_3$ (e, f) determined at 2.5 keV impact energy. EELS spectra are collected in steps of 1.0° from 1.0° to 9.0° for CF_3Cl, and in steps of 0.5° from 1.0° to 9.5° for CF_2Cl_2 and $CFCl_3$. The spectra collected above 4° have been smoothed for clarity. The dipole EELS spectra of CF_3Cl, CF_2Cl_2, and $CFCl_3$ obtained from literature [33] are shown as dashed lines and have been placed at an approximate momentum transfer (K) position (0.1 a.u.), which corresponds to the lower limit of our scale. The impact-scattering (large momentum transfer) domain is emphasized in (a), (c), and (e), while the dipole-scattering domain is depicted in (b), (d), and (f).

rise to a more rapid drop-off with the momentum transfer (Fig. 3).

4.1. Non-dipole HOMO→LUMO excitation in CF_3Cl

In order to demonstrate the momentum-transfer dependence of the spectral features observed in the valence shell of CF_3Cl, we show in Fig. 4 a selected number of angle-resolved EELS spectra collected at a series of scattering angles [32]. Our small-angle spectrum (Fig. 4a) is found to be consistent with the earlier dipole EELS [50,51] and photoabsorption data [52–54], and the observed features may be

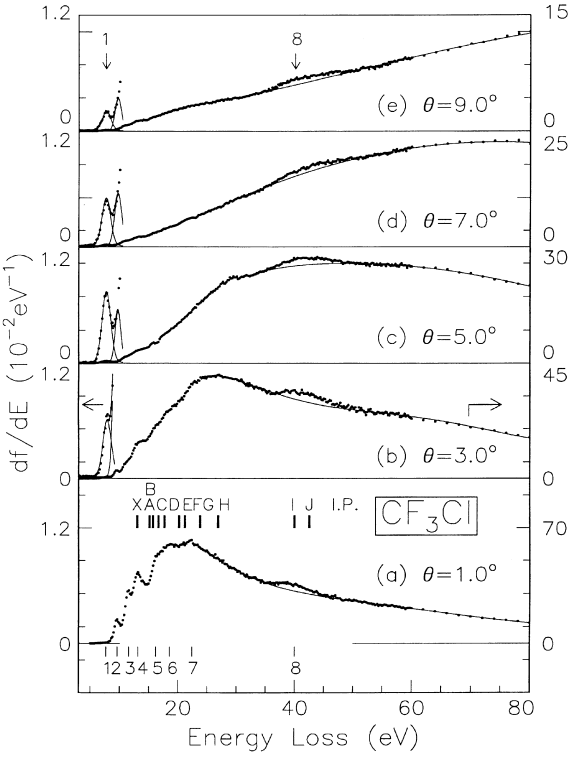

Fig. 4. Angle-resolved electron energy loss spectra of the valence shell of CF_3Cl at 2.5 keV impact energy and θ=(a) 1.0°, (b) 3.0°, (c) 5.0°, (d) 7.0°, and (e) 9.0°. The intensity variation of the weak peak at 7.7 eV (feature 1) is shown using an expanded scale (left axis) while the rest of the spectrum corresponds to the right vertical scale. Two Gaussian profiles are used to estimate the intensities of feature 1 and its neighbour, respectively, by a curve-fitting procedure, as illustrated in (b) to (e). The experimental vertical ionization potentials (I.P.s) of the X–J states (vertical bars) are obtained from the literature [33].

assigned to the appropriate dipole-allowed Rydberg transitions. In particular, features 2 to 7 have been assigned to the 5e→4s (9.5 eV), 5e→5s and/or 5e→3d (11.5 eV), 4e→4s and/or $1a_2$→4p (13.5 eV), $4a_1$→4s (16.5 eV), $4a_1$→5s and/or 2e→4p (18.5 eV), and $2a_1$→3s (22.3 eV) transitions, respectively. In addition to these 'optical' features, our angle-resolved spectra recorded at the larger angles clearly indicate the presence of a weak broad feature at 40.5 eV (feature 8), which has also been reported previously [50,51]. The broad 40.5 eV feature likely contains the ionization edges of both inner-valence $(1e)^{-1}$ and $(1a_1)^{-1}$ states, which are at 40.0 and 42.5 eV, respectively. This broad peak (located at 37–42 eV) is also a common feature among other members of the CFC series (including CF_2Cl_2 and $CFCl_3$) [33]. The strong correlation between the intensity of this broad peak and the number of F atom(s) in the CFC molecules further suggests that these broad features are related to transitions near the ionization onsets of the inner-valence F 2s orbitals [50,51]. Finally, the spectra clearly reveal the presence of a 'new' state at 7.7 eV [32], i.e. at an energy that is 1.7 eV below the onset of the predominantly dipole-allowed Rydberg states observed in the 1° spectrum (Fig. 4a).

To illustrate in more detail the interesting momentum-transfer dependence of the newly observed non-dipole feature at 7.7 eV, we have estimated its peak intensity with a Gaussian profile, after removing an appropriate contribution from the nearby discrete dipole transition(s), in each of the angle-resolved spectra. Fig. 5 shows the resulting GOS profile [32], which clearly contains a relative maximum away from zero momentum transfer (i.e. at $K^2 \approx 1.0$ a.u.), characteristic of a non-dipole transition. Only a limited number of non-dipole electronic transitions in the valence shell have been previously characterized by means of GOS measurements. In particular, the GOS profile of the well known Lyman–Birge–Hopfield band in N_2 at 9.3 eV (Fig. 2) was found to have a maximum at $K^2 \approx 0.8$ a.u. and has been identified as a quadrupole-allowed $a^1\Pi_g \leftarrow X^1\Sigma_g^+$ transition [13–18,40]. In addition, a second quadrupole transition at 31.4 eV in N_2 has also been observed with the GOS maximum at $K^2 \approx 1.1$ a.u. and could be attributed to the $2\sigma_g \rightarrow 1\pi_g$ single-excitation and discrete double-excitation transitions [13–17,55]. Other non-

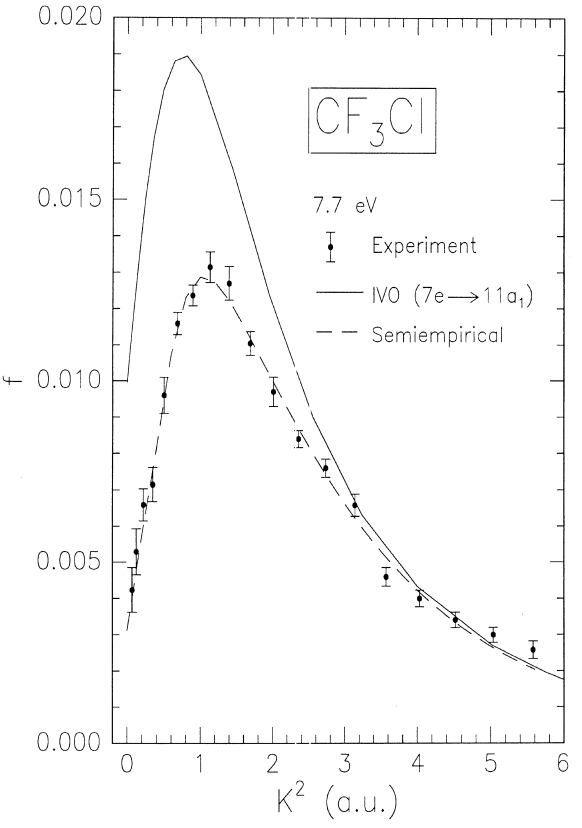

Fig. 5. Absolute generalized oscillator strength (f) as a function of momentum transfer (K) squared for the 7.7 eV transition in CF_3Cl. The dashed curve corresponds to a semiempirical polynomial fit based upon the Lassettre series expansion. The solid line represents the result of an improved virtual orbital (IVO) calculation [32].

dipole transitions have also been found in the valence shells of C_2H_2 [19], benzene [20], and *p*-difluorobenzene [21]. These studies generally demonstrate that dipole-allowed non-Rydberg transitions have maximum GOS at $K=0$ while non-dipole transitions (quadrupole or octupole) usually have maximum GOS at non-zero K values (usually ~1 a.u. for most non-dipole, valence-shell transitions observed to date). Fig. 5 therefore gives direct evidence for a non-dipole, non-Rydberg transition lying below all previously reported dipole-allowed transitions in CF_3Cl [32]. Furthermore, we can also derive the absolute DOS by fitting the measured GOS profile using the Lassettre power series expansion (Eq. (6)) [7–9], the coefficients derived from which are consistent with those of a predominantly quadrupole transition.

Also shown in Fig. 5 are the results of ab initio GOS calculations for the $^1E\leftarrow{}^1A_1$ ($7e\rightarrow 11a_1$) excitation [32]. The calculations employed an improved virtual orbital (IVO) representation [56] of the ^1E state and a Hartree–Fock ground state. Although the calculated GOS is somewhat larger, reasonably good agreement is evidently obtained between theory and experiment for the shape, with the minima of both the theoretical and experimental GOS curves at zero momentum transfer and maxima at $K^2\approx 1$ a.u. The finite DOS value derived by using the Lassettre series is consistent with the small value of the computed dipole oscillator strength. In addition, using a separate single-excitation CI excited-state calculation for the excited state with a 6-31G (6-31^{++}G**) basis set and an internally optimized geometry for CF_3Cl [57], we also found the transition energy of the $^1E\leftarrow{}^1A_1$ transition to be 8.59 eV (9.01 eV) with a small dipole transition moment of 0.0024 (0.0064) [32]. The reasonably good agreement of the experimental transition energy (7.7 eV) and the DOS value (0.003) with the calculations provides further support for the assignment of the 7.7 eV transition as the $^1E\leftarrow{}^1A_1$ excitation.

The nature of this lowest-energy singlet transition can be understood in terms of simple molecular orbital picture involving the excitation of an electron from the highest occupied molecular orbital (HOMO), 7e, with Cl 3p lone-pair character ($n_{Cl\ 3p}$), into the lowest unoccupied molecular orbital (LUMO), $11a_1$, with C–Cl σ* character (σ^*_{C-Cl}). Fig. 6 compares the contour maps of the wavefunction densities of the initial-state and final-state orbitals involved in this type of $n_{Cl\ 3p}\rightarrow\sigma^*_{C-Cl}$ transitions for CF_3Cl (and CHF_2Cl, see later) [36]. The contour maps were generated from ab initio self-consistent field (SCF) wavefunctions obtained by GAUSSIAN 90 with a 6-31G basis set and internally optimized geometries [57]. The Cl 3p lone-pair nature of the doubly degenerate orbitals, labeled as 7e and 7e′, in CF_3Cl is clearly illustrated in Fig. 6e and f, respectively, while the $11a_1$ orbital shown in Fig. 6d is seen to consist of antibonding overlap between the C(2s, $2p_x$) and Cl $3p_x$ atomic orbitals, with its characteristic nodal plane bisecting the C–Cl bond. In the case of the $n_{Cl\ 3p}\rightarrow\sigma^*_{C-Cl}$ ($7e\rightarrow 11a_1$) transi-

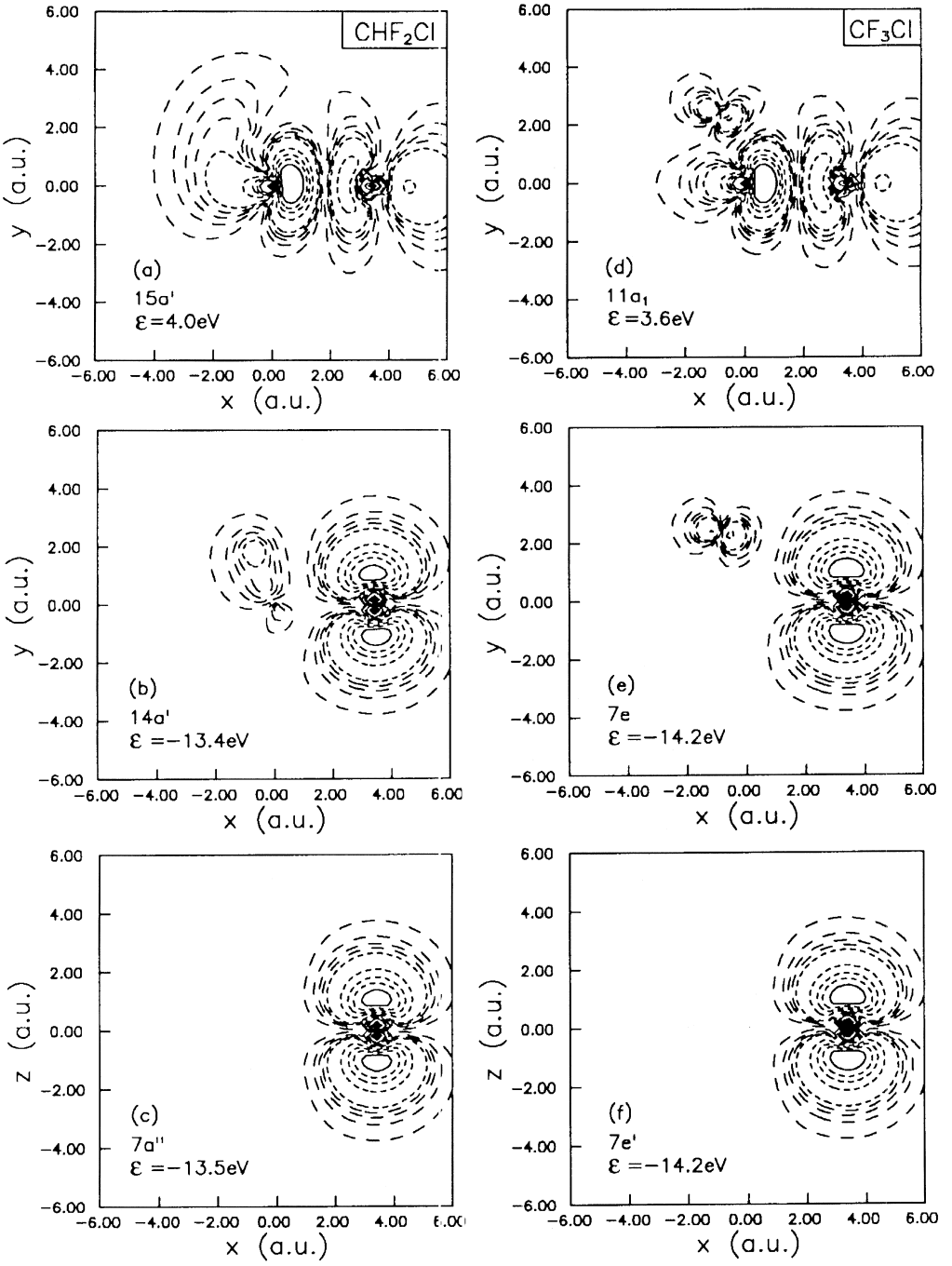

Fig. 6. Two-dimensional wavefunction density contour maps for (a) the 15a′, (b) 14a′ and (c) 7a″ orbitals of CHF_2Cl, and for (d) the $11a_1$, (e) 7e and (f) 7e′ orbitals of CF_3Cl. The molecules are oriented with the carbon atoms located at the origin. The H–C–Cl group in CHF_2Cl and an F–C–Cl group in CF_3Cl have been positioned on the *xy* plane with the C–Cl bond oriented along the *x* axis. The contour values are 0.1, 0.3, 0.5, 0.7 (dashed lines), 1, 3, 5, 7 (dotted lines), 10, 30, 50, 70 and 90% (solid lines) of the maximum density. The contour maps are calculated using ab initio SCF wavefunctions of 6-31G quality generated with internally optimized geometries [57]. The molecular orbital symbols and calculated SCF orbital energies (ε) are also shown in the plots (note that a positive value for the orbital energy indicates a virtual orbital).

tion in CF_3Cl, the overlap between the initial-state and final-state orbital wavefunctions occurs mostly at the Cl site. The transition moment of this $n_{Cl\ 3p} \rightarrow \sigma^*_{C-Cl}$ electronic transition is therefore expected to resemble that of a p-to-p transition in a Cl atom, which readily explains the observed quadrupole nature of this transition.

In Fig. 7, we show the potential energy curves of the $^1A_1$ and ^1E states along the C–Cl bond direction, generated by using the 6-31G and 6-31^{++}G** basis sets [32]. Clearly, other than the apparent shift in the potential energy curve to a lower energy for the 6-31^{++}G** basis set, there is no obvious difference in the general shapes of the potential energy curves obtained by these two basis sets. Since the direct product table for the symmetry group C_{3v} indicates that the $^1E \leftarrow {}^1A_1$ transition is both dipole-allowed and quadrupole-allowed, the relatively small dipole transition moment observed earlier therefore suggests that this transition can be attributed predominantly to quadrupole interactions, which is consistent with the dominant molecular orbital coefficients. Of particular interest shown in the simple potential energy diagram (Fig. 7) is that a vertical transition originated from the ground vibrational level of the $^1A_1$ state terminates at the repulsive part of the potential energy curve of the ^1E state above its dissociation limit. Fig. 7 therefore provides qualitative support for the predissociative nature of the 'metastable' ^1E state and that electronic transition to this state would lead to the breakage of the C–Cl bond.

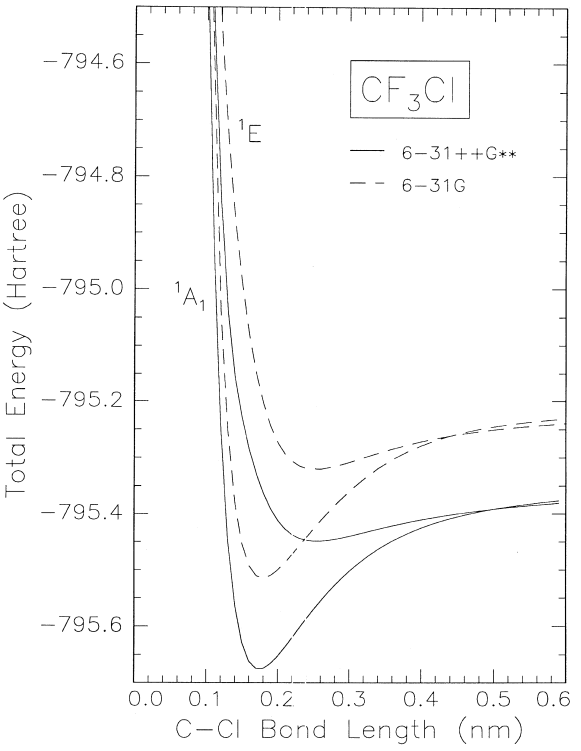

Fig. 7. Potential energy diagram along the C–Cl bond direction for the $^1A_1$ and ^1E states of CF_3Cl. The potential energy curves of the two states are obtained using single-excitation configuration interaction excited-state calculations with 6-31G (dashed lines) and 6-31^{++}G** (solid lines) basis sets [57]. Except for the C–Cl bond length, all other structural parameters obtained in an internally optimized geometry are held constant in the potential energy curve calculations.

4.2. Analogous non-dipole electronic transitions in HCF_2Cl and other CFC substitutes

The large-scale consumption of CFCs (as refrigerants, aerosol propellants, and semiconductor etchants, etc.) in many industrial applications [48,49] has become a major environmental concern because of their destructive effect on ozone in the stratosphere [58]. Many of the popular CFCs, including CF_3Cl (Section 4.1) [32], CF_2Cl_2 and $CFCl_3$ [33], as well as CF_4 and CCl_4 [34], have been replaced with the more 'environment-friendly' substitutes, which usually consist of HCFCs including CHF_2Cl [36], $CHFCl_2$ [37], CHF_3 and $CHCl_3$ [38] as well as their derivatives. Unlike the simple CFCs, however, the electronic structure and photochemistry of HCFC molecules are less well understood. For instance, there is no information on the important excitation cross sections of low-lying or any other electronic transitions, which, like their counterparts in CFCs, may play a key role in the relevant atmospheric and industrial processes. A few of these $n \rightarrow \sigma^*$ transitions in the 6–9 eV region for some of the more common CFC and HCFC molecules have been reported as 'weak' features in the early vacuum ultraviolet photoabsorption [52–54] and high-resolution dipole EELS studies [50,51]. We have conducted a series of comparative studies involving HCFCs [36–38] with the goal to elucidate the effects of halogen content and symmetry change, e.g. from C_{3v} (CF_3Cl) to C_s (CHF_2Cl), on the GOS profiles and

the nature of this type of $n \rightarrow \sigma^*$ and other relevant low-lying electronic excitations.

The angle-resolved EELS spectra of CHF_2Cl (Freon 22) [36] shown in Fig. 8 reveal the similarity of its electronic structure to that of its CFC counterpart (CF_3Cl, Fig. 4). Except for the weak feature at 8.0 eV, most of the observed features below the ionization edge could again be attributed to Rydberg transitions [36]. The GOS profile of this feature in CHF_2Cl is compared with that of the 7.7 eV feature in CF_3Cl in Fig. 9. Evidently, the two GOS profiles appear to be very similar both in shape and magnitude. The maximum at $K^2 \approx 1$ a.u. in the GOS profile of the 8.0 eV feature in CHF_2Cl (like that of the 7.7 eV feature in CF_3Cl) is therefore characteristic of the non-dipole nature of the transitions involved. We can again perform a single-excitation CI excited-state calculation using a 6-31G basis set and an internally optimized geometry [57] for CHF_2Cl to identify the nature of the transitions involved [36]. Only singlet-to-singlet electronic transitions are calculated because the contribution to the low-lying 8.0 eV feature from the spin-forbidden singlet-to-triplet transitions is negligible at the high impact energy (2.5 keV) employed in our experiment. The calculation shows that the feature at 8.0 eV can be

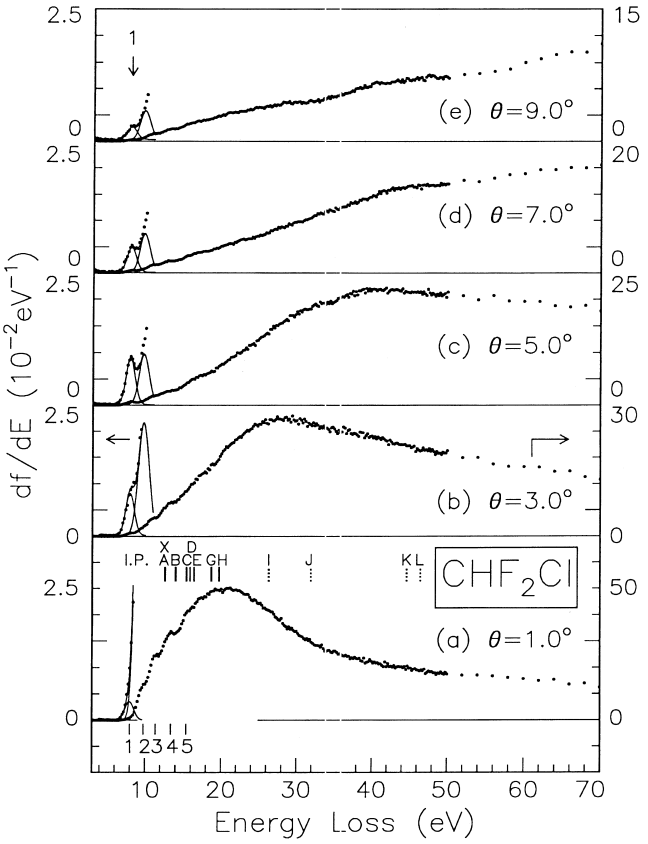

Fig. 8. Angle-resolved electron energy loss spectra of the valence shell of CHF_2Cl at 2.5 keV impact energy and θ = (a) 1.0°, (b) 3.0°, (c) 5.0°, (d) 7.0°, and (e) 9.0°. The intensity variation of the weak peak at 8.0 eV (feature 1) is shown using an expanded scale (left axis) while the rest of the spectrum corresponds to the right vertical scale. Three Gaussian profiles are used to estimate the intensities of feature 1 (8.0 eV) and two neighbouring discrete states (at 9.8 eV and 11.4 eV) in a curve-fitting procedure (note the fitting results of the third Gaussian peak are not shown). The experimental vertical ionization potentials (I.P.s) of the X–H states (vertical bars) are obtained from the literature [36]. State F is not labelled because of its ambiguity. The I.P.s for states I–L (dotted vertical bars) are obtained from an ab initio SCF calculation with a 6-31G basis set [57].

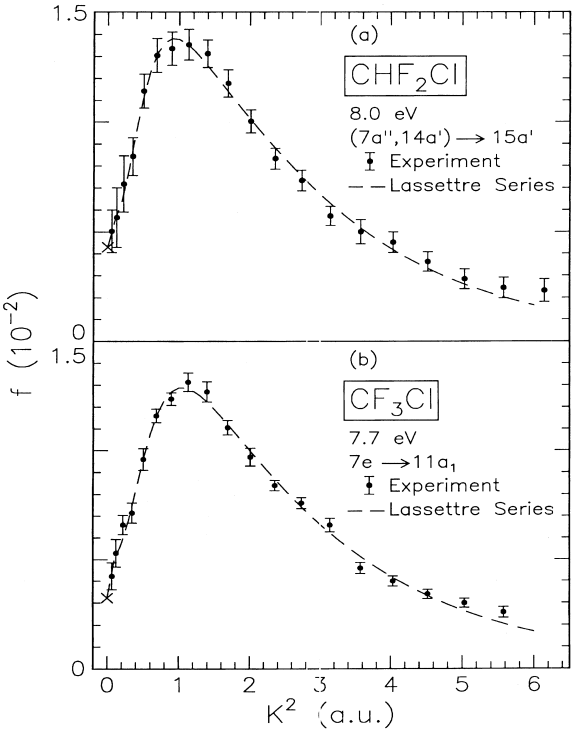

Fig. 9. Absolute generalized oscillator strength (f) as a function of momentum transfer (K) squared for (a) the 8.0 eV feature in CHF_2Cl and (b) the 7.7 eV feature in CF_3Cl. The dashed curves correspond to semiempirical polynomial fits based upon the Lassettre series expansion. Projected dipole oscillator strengths are indicated by crosses (×).

adequately assigned as two predominant transitions from the ground state to the $^1A'$ ($14a' \rightarrow 15a'$) and $^1A''$ ($7a'' \rightarrow 15a'$) excited states, which correspond respectively to electronic transitions from two essentially Cl 3p lone-pair orbitals (the HOMO 14a′ and next HOMO 7a″) to a σ^*_{C-Cl} antibonding orbital (the LUMO 15a′) [36]. The corresponding calculated transition energies from the ground state to the two excited states, $^1A'$ and $^1A''$, are 8.62 and 8.68 eV respectively, which are in good accord with the experimental excitation energy of 8.0 eV. The total calculated DOS of 0.0052 for the two excited states (0.0039 for the $^1A'$ state and 0.0013 for the $^1A''$ state) is also in good agreement with the small f_0 value of 0.0043 derived experimentally (Eq. (6)) [36]. The agreements obtained in the excitation energy and in the DOS between the calculation and experiment therefore provide strong evidence for the assignment of the $14a' \rightarrow 15a'$ and $7a'' \rightarrow 15a'$ electronic transitions to the observed low-lying feature at 8.0 eV in CHF_2Cl.

We can also understand the similarities in the GOS profiles between these HOMO→LUMO transitions in CHF_2Cl and CF_3Cl by examining the electron densities of the orbitals involved in the two molecules. Fig. 6a shows the antibonding σ* character of the 15a′ orbital, while Fig. 6b and c illustrate the lone-pair nature of the 14a′ and 7a″ orbitals [36], which consist mainly of the in-plane Cl $3p_y$ and out-of-plane Cl $3p_z$ orbitals, respectively. The contour maps of the σ^*_{C-Cl} antibonding (15a′) and $n_{Cl\ 3p}$ lone-pair (14a′ and 7a″) orbitals in CHF_2Cl (Fig. 6a–c) depict striking similarities to those of the corresponding orbitals in CF_3Cl (Fig. 6d–f). Essentially the same descriptions for the antibonding and lone-pair orbitals and for the quadrupole nature of the p-to-p type transitions between these orbitals in CF_3Cl can also be applied to those in CHF_2Cl. Given these similarities, it is therefore not surprising to find that the potential energy curves along the C–Cl bond direction calculated using the single-excitation CI excited-state approach for these $n_{Cl\ 3p} \rightarrow \sigma^*_{C-Cl}$ transitions in CHF_2Cl [36], shown in Fig. 10, would also be similar to those for CF_3Cl (Fig. 7). It is also obvious from this potential energy diagram (Fig. 10) that the electronic transitions, $14a' \rightarrow 15a'$ and $7a'' \rightarrow 15a'$, may both lead to the dissociation of the C–Cl bond. The results of these potential energy curve calculations strongly suggest that dissociation of the C–Cl bond is a common consequence of the $n_{Cl\ 3p} \rightarrow \sigma^*_{C-Cl}$ transitions in CHF_2Cl and CF_3Cl.

Our studies on the GOS profiles of the $n_{Cl\ 3p} \rightarrow \sigma^*_{C-Cl}$ transitions in the common CFCs (CF_3Cl, CF_2Cl_2, and $CFCl_3$) [33] and their more ‘environment-friendly’ HCFC homologs (CHF_2Cl [36], $CHFCl_2$ [37], and $CHCl_3$ [38]) have revealed several interesting empirical trends: (1) the relative maximum intensity of the GOS profile within the aforementioned CFC and HCFC series increases almost proportionally with increasing chlorine content, and (2) the relative amount of the dipole component (peak at $K=0$) to non-dipole component (peak at $K^2 \approx 1$ a.u.) also increases with increasing chlorination. Figs. 11 and 12 illustrate these general

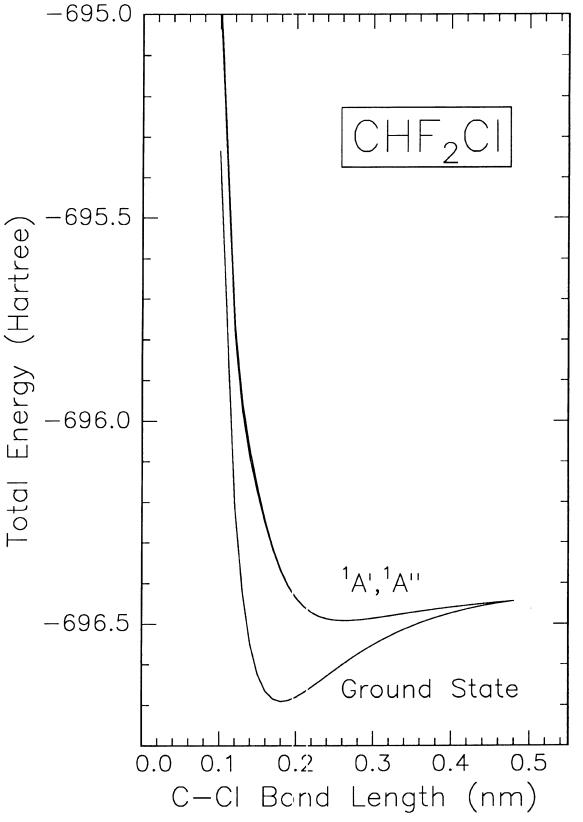

Fig. 10. Potential energy diagram along the C–Cl bond direction for the ground state and the two lowest-lying excited states (^{1}A′ and ^{1}A″) of CHF_2Cl. The potential energy curves are obtained using single-excitation configuration interaction excited-state calculations with a 6-31G basis set [57]. Except for the C–Cl bond length, all other structural parameters obtained from an internal geometry optimization are held constant in the potential energy curve calculations.

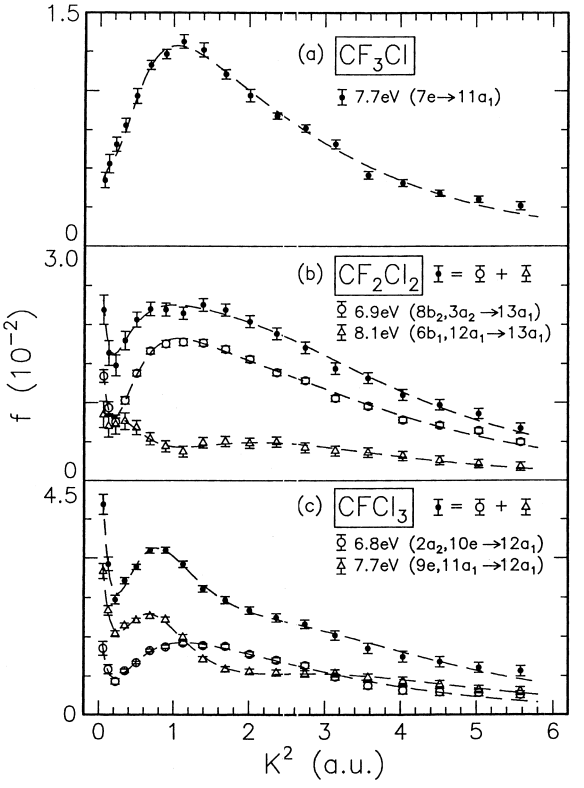

Fig. 11. Absolute generalized oscillator strength (f) as a function of momentum transfer (K) squared for (a) the 7.7 eV feature in CF_3Cl, (b) the 6.9 and 8.1 eV features in CF_2Cl_2, and (c) the 6.8 and 7.7 eV features in $CFCl_3$ [33]. The dashed curves correspond to semiempirical polynomial fits based upon the Lassettre series expansion.

trends in the GOS profiles of the HOMO→LUMO transitions for the CF_3Cl, CF_2Cl_2, and $CFCl_3$ series [33] and for the CHF_2Cl, $CHFCl_2$ and $CHCl_3$ series, respectively [37]. In particular, the maxima for the respective GOS profiles approximately follow the 1:2:3 ratio, in concert with increasing chlorination. For instance, the relative contribution from the dipole component in the HCFC series also increases with increasing chlorine content, with the strongest dipole peak (at $K=0$) in $CHCl_3$, which is also consistent with the relative ratio of the calculated (experimental) DOS values, 1:3.8:8.8 (1:5.8:13.4), for CHF_2Cl:$CHFCl_2$:$CHCl_3$ (Fig. 12). Although there are close correspondences in the GOS profiles of the HOMO→LUMO transitions for CHF_2Cl (Fig. 12a) and CF_3Cl (Fig. 11a) and for $CHCl_3$ (Fig. 12c) and $CFCl_3$ (Fig. 11c), the similarities between $CHFCl_2$ and CF_2Cl_2 are less striking, with a considerably sharper GOS secondary maximum in $CHFCl_2$ (Fig. 12b) relative to the broad peak in CF_2Cl_2 (Fig. 11b) [33]. The trend observed for the relative ‘dipole to non-dipole’ contributions for these transitions suggests that molecular symmetry plays a key role in defining the contributions from different types of transitions to the GOS profile. For instance, the excited states of a more ‘cage-like’ molecule such as $CHCl_3$ may be more susceptible to distortion due to Jahn–Teller effects, which in turn give rise to the more intense $K=0$ (dipole) peak in the corre-

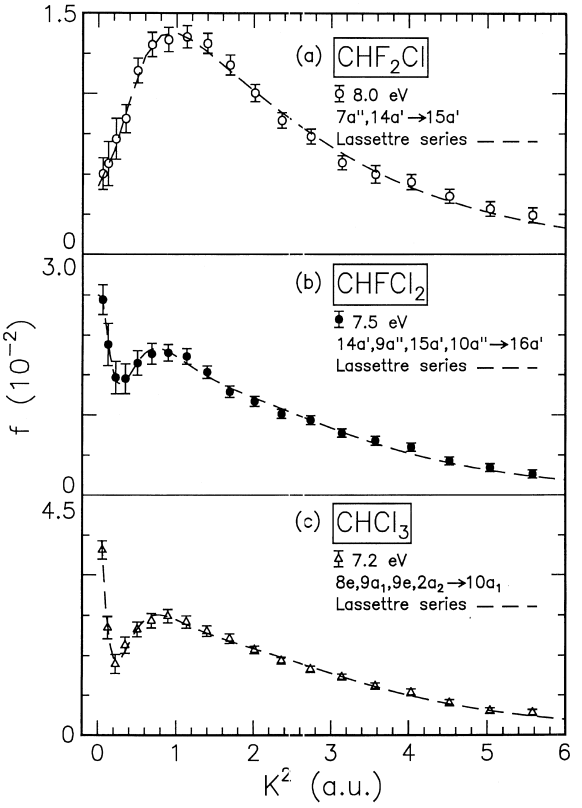

Fig. 12. Absolute generalized oscillator strength (f) as a function of momentum transfer (K) squared for (a) the 8.0 eV feature in CHF_2Cl, (b) the 7.5 eV feature in $CHFCl_2$, and (c) the 7.2 eV feature in $CHCl_3$ [37]. The dashed curves correspond to semiempirical polynomial fits based upon the Lassettre series expansion.

sponding GOS profile. Finally, a noteworthy trend obtained from these series of angle-resolved EELS studies is that most of the $n_{Cl\ 3p}\rightarrow\sigma^*_{C-Cl}$ transitions in the aforementioned CFC [33] and HCFC molecules [36–38] contain non-dipole interactions that lead to the dissociation of the C–Cl bond. In particular, simple potential energy curve calculations suggest that the following $n_{Cl\ 3p}\rightarrow\sigma^*_{C-Cl}$ transitions are predissociative: the $7e\rightarrow11a_1$ transition at 7.7 eV in CF_3Cl (Fig. 7), $(3a_2, 8b_2)\rightarrow13a_1$ transitions at 6.9 eV in CF_2Cl_2 [33], $10e\rightarrow12a_1$ transition at 6.8 eV in $CFCl_3$ [33], and $2t_1\rightarrow7a_1$ transition at 7.2 eV in CCl_4 [34], as well as the $(7a'', 14a')\rightarrow15a'$ transitions at 8.0 eV in CHF_2Cl (Fig. 10), $(10a'', 9a'')\rightarrow16a'$ transitions at 7.5 eV in $CHFCl_2$ [37], and $9e\rightarrow10a_1$ transition at 7.2 eV in $CHCl_3$ [38]. The predissociative nature of the HOMO→LUMO transitions in these molecules is apparently quite common and clearly of interest to the understanding of photochemical and electron-induced processes in the upper atmosphere and in plasma-related industrial applications.

5. Application to GOS measurements of inner-shell transitions

In addition to the spectroscopic interest in the effects of molecular symmetry and ligand substitution on molecular GOS profiles of the low-lying excited states in the valence shell, the $CF_{4-n}Cl_n$ ($n=0$–4) series also represents prototypical systems for the investigation of 'cage' effects and shape resonances in inner-shell electronic excitation [59]. In contrast to the large amount of optical and dipole EELS data in the inner shells [60–62], only a limited number of angle-resolved EELS studies have been made in this energy region. In particular, Shaw et al. reported the first observation of a dipole-forbidden singlet-to-triplet N $1s\rightarrow\pi^*$ $2p_{3/2}$ transition in N_2 using low-energy electron impact below 600 eV [22]. Camilloni et al. showed that the GOS profiles of the N $1s\rightarrow\pi^*$ 2p excitations in N_2, NO and N_2O obtained by angle-resolved EELS at 1.4 and 3.4 keV [23] have a similar dipole-dominated shape to one another, which suggests the similarity in inner-shell excitations in these molecules. The GOS profiles of the predominant dipole-allowed C $1s\rightarrow2\pi_u$ transitions in CO_2 [25] and in C_2H_2 [26] were obtained at an impact energy of 1.29 keV by de Souza and coworkers, who also gave detailed theoretical investigation of relaxation effects in the determination of excited-state wavefunction. In 1993, we reported the first GOS measurement of a non-dipole inner-shell transition at high impact energy [28]; and this work has generated a renewed interest in angle-resolved EELS studies of the inner shells [29,30]. In particular, the GOS profile of the S $2p\rightarrow6t_{1u}$ transition in SF_6 was found to have a maximum at higher momentum transfer ($K>2.5$ a.u.), in marked contrast to the GOS profiles of most of the non-dipole valence-shell transitions observed to date (where the GOS maxima usually occur at ~1 a.u.). This work further illustrates the qualitative difference in the

momentum-transfer dependence of the GOS profile of the S $2p \rightarrow 6t_{1u}$ transition, in comparison with those of the dipole-allowed below-edge discrete and above-edge shape resonance states [28]. Finally, the recent high resolution studies involving GOS measurements to very high momentum transfer values by Hitchcock and coworkers are providing new insights into spin exchange transitions in C_2H_2, C_2H_4 and C_6H_6 [27], singlet vs. triplet potential surfaces in the C 1s excitation of CO [24], and more comprehensive S 2p [29,30] and S 2s excitations in SF_6 [31].

In the remainder of this article, we shall highlight some of the unique spectroscopic features that could be obtained from angle-resolved EELS studies of the inner shells, using the more prominent below-edge features in the C 1s and Cl 2p shells of CF_3Cl as our examples [35]. In particular, by determining the GOS profiles of the respective transitions to the σ^*_{C-Cl} orbital from the C 1s or Cl 2p shell, it may be possible to examine atomic-site-specific effects relating to core-level relaxation. Furthermore, the extent of chlorination and the change in molecular symmetry in inner-shell transitions would also be of interest.

5.1. Excitations from carbon 1s shell of CF_3Cl

Fig. 13 shows the angle-resolved EELS spectra of the carbon 1s shell at three different scattering angles. The 1° spectrum (Fig. 13a) for the C 1s region is in good accord with the corresponding high-resolution dipole EELS spectra reported by Zhang et al. [61]. The more prominent features have been assigned as transitions from the C 1s orbital to

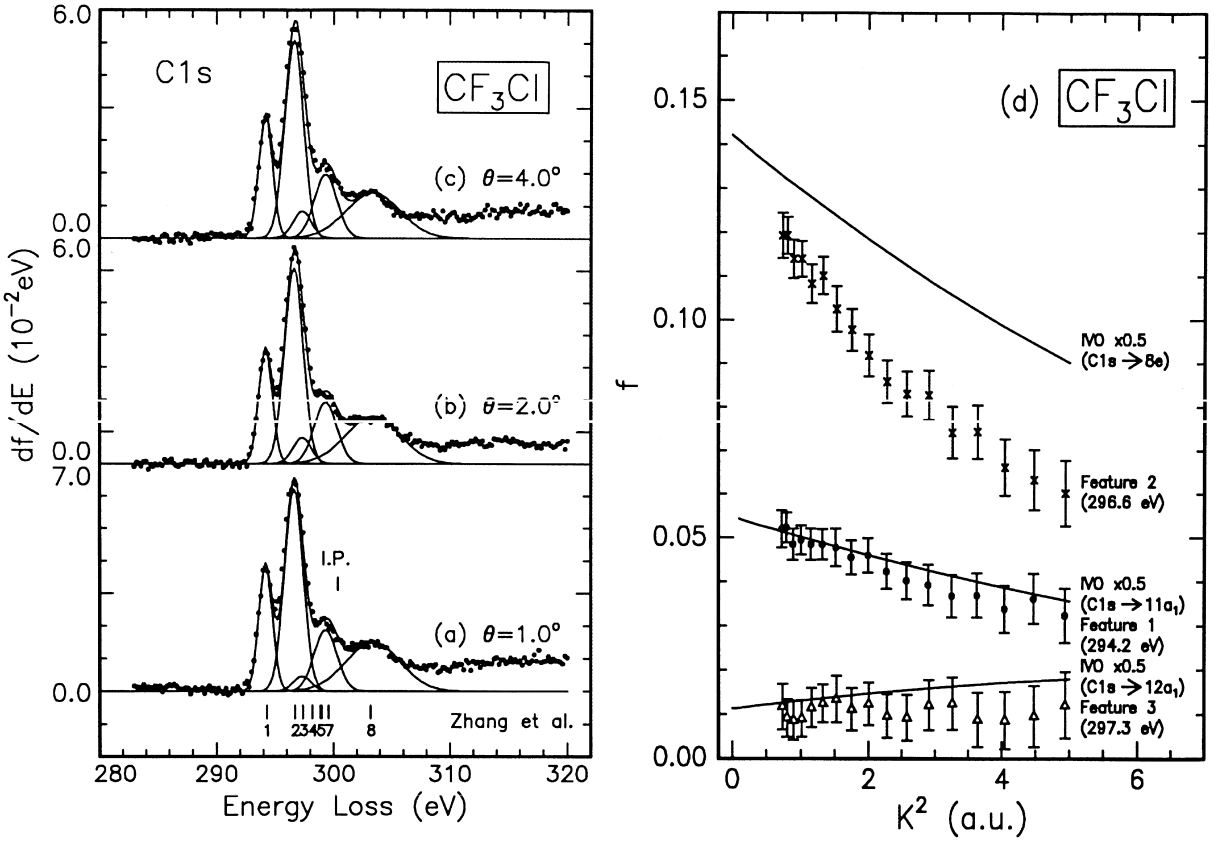

Fig. 13. Angle-resolved electron energy loss spectra of the carbon 1s shell of CF_3Cl measured at 2.5 keV impact energy and θ = (a) 1.0°, (b) 2.0°, and (c) 4.0°. (d) Absolute generalized oscillator strength (f) as a function of momentum transfer (K) squared for the three lowest-lying C 1s pre-edge transitions [35]. The solid lines represent the results of an improved virtual orbital (IVO) calculation [63].

the LUMOs with σ^*_{C-Cl} character and other unoccupied orbitals of σ^*_{C-F} character, as well as to various Rydberg orbitals [35]. In addition to the below-edge features, evidence of shape-resonance states can also be found within 10 eV of the continuum region above the C 1s edge of our angle-resolved EELS spectra for $CF_{4-n}Cl_n$ ($n=0$–4) [35]. Other near-edge (XANES type) states are also evident above the C 1s and Cl 2p edges. Like the below-edge features, these above-edge features are found to decrease in intensity with increasing scattering angle (momentum transfer), without noticeable change in the general shape from that of the 1° spectrum. Except for a general reduction in the overall intensity, there is evidently no discernible difference in the general shape of the electron-impact excitation structure at the larger scattering angle. The lack of a strong angular dependence is characteristic of many of the inner-shell transitions that we studied thus far, in marked contrast to the relatively rapid variation with the momentum transfer commonly observed for valence-shell transitions.

Although the below-edge region could be fitted with a large number of energy loss features reported by Zhang et al. (Fig. 13a) [61], only the lowest lying features that can be reliably resolved from the rest of our EELS spectrum (i.e. the first three pre-edge features) are used to determine the GOS profiles by using a Gaussian deconvolution technique [35]. As we have illustrated earlier, the main features of a GOS profile can be understood qualitatively in terms of Fourier transform of the spatial overlap between the initial-state and the final-state wavefunctions (Eq. (4)). In the case of inner-shell transitions, the initial-state wavefunctions are localized at the respective atomic centres. The GOS profile is therefore sensitive to the bonding environment in the preselected 'small' spatial region at the respective atomic sites of the unoccupied excited-state wavefunction. In Fig. 13d, the experimental GOS profiles of the three lowest-lying pre-edge features are compared with the results of ab initio GOS calculations that employed an IVO representation of the excited states discussed in Section 4.1 [63]. Although the magnitudes of the calculated GOS curves are off by about a factor of two, generally good agreement in the shapes of the GOS profiles has been obtained between the theory and experiment. The calculations provide general support for the assignments of the observed below-edge C 1s excitation features. In particular, the GOS profiles of both feature 1 (at 294.2 eV) and feature 2 (at 296.6 eV) are found to decrease with increasing momentum transfer, and these features may correspond to the dipole-allowed C $1s\rightarrow 11a_1$ and C $1s\rightarrow 8e$ transitions, respectively. The dipole nature of the $s\rightarrow p$ type transitions is consistent with the nature of the final-state orbitals: $11a_1$, which corresponds to a σ^*_{C-Cl} orbital (Fig. 6), and 8e and $12a_1$, both of which involve predominantly σ^*_{C-F} overlaps. Because of the localized nature of the initial-state C 1s orbital, the similarity between the GOS profiles suggests that the σ^*_{C-Cl} and σ^*_{C-F} virtual orbitals both involve similar p-type components at the C site, which are consistent with the finite MO coefficients for C (p_z) in $11a_1$ and $12a_1$, and that for C (p_x, p_y) in 8e as given by a standard restricted Hartree–Fock SCF calculation [57]. It is of interest to note that the GOS profiles for these C 1s excitations remain relatively intense even at $K^2\approx 5$ a.u., which is a common feature characteristic of inner-shell transitions because the higher K components correspond to 'close' collisions that occur near the nuclear centre. The GOS profile of feature 3 (at 297.3 eV), on the other hand, appears to be essentially flat within the experimental K range. Although the small intensity of this feature does not allow us to make a definitive assignment, it is of interest to note the similarity between the experiment and the calculated GOS profile of the C $1s\rightarrow 12a_1$ transition. Within the experimental statistics, the calculated GOS profile of C $1s\rightarrow 12a_1$ appears to increase slowly with K, which suggests possible contributions from non-dipole interactions. The general behaviour of the calculated GOS curve is similar to that of the observed GOS profile of the non-dipole S $2p\rightarrow 6t_{1u}$ transition in SF_6 [28]. Extending the GOS measurement to a higher momentum transfer range will therefore be of great interest in these cases.

It is of interest to compare the overall shapes of the GOS profiles of the C $1s\rightarrow\sigma^*_{C-Cl}$ (LUMO) features of the CF_3Cl, CF_2Cl_2 and $CFCl_3$ series [35]. In particular, the GOS profile of the C $1s\rightarrow 11a_1$ feature of CF_3Cl (Fig. 13d) is found to be significantly broader than the GOS profiles of the corresponding C $1s\rightarrow$LUMO features in CF_2Cl_2 and $CFCl_3$ (not shown) [35]. The apparent increase in the

higher K components of the GOS profile of the C $1s\rightarrow 11a_1$ feature in CF_3Cl is clearly related to the differences in the final-state orbitals. In particular, only the σ^* density overlap of CF_3Cl is directed along the C–Cl bond direction, while the other σ^* overlaps of CF_2Cl_2 and $CFCl_3$ are distorted from the C–Cl bond direction due to the presence of the other chlorine atom(s). The more abrupt variation of the density overlaps in the $11a_1$ orbital may also introduce the observed higher K components. For CCl_4, the observed GOS profile of the first feature consists of contributions from both the C $1s\rightarrow 7a_1$ (LUMO) and C $1s\rightarrow 8t_2$ transitions [35], which make it difficult to interpret the contribution due to the C $1s\rightarrow 7a_1$ transition alone. It is of interest to note that the apparent width of the observed intensity within the accessible experimental momentum transfer range of the GOS profile for CCl_4 is found to be intermediate between that of the corresponding GOS profile of CF_3Cl and those of CF_2Cl_2 and $CFCl_3$. The estimated DOS value to which the GOS profile of CCl_4 appears to be converging is found to be higher than those of CF_3Cl, CF_2Cl_2 and $CFCl_3$, which are generally similar to one another. The higher DOS value for CCl_4 is indicative of the strongly dipole-allowed nature of the C $1s\rightarrow 8t_2$ transitions.

5.2. Non-dipole excitations from the chlorine 2p shells of CF_3Cl

Fig. 14 compares the GOS profile of the Cl $2p_{3/2}\rightarrow 11a_1$ transition (feature 1) with that of the Cl $2p_{1/2}\rightarrow 11a_1$ transition (feature 2) in CF_3Cl [35]. Except for the small offset in the intensity, the two GOS profiles are similar in shape to each other, to within the statistical accuracy of the data. The ratio of the absolute magnitudes of the two GOS profiles follows closely that of the $2J+1$ degeneracies of the initial-state orbitals $2p_{3/2}$ and $2p_{1/2}$. Our present experiment is apparently not sufficiently sensitive to differentiate contribution due to spin effects, and further refinement in the experimental technique is necessary to reduce the statistical errors. Since the $11a_1$ orbital consists predominantly of σ^*_{C-Cl} overlap with strong s and p components at both the Cl and C sites (Fig. 6) [36], the peak near the K origin and that with maximum at $K^2\approx 1.2$ a.u. therefore correspond to the dipole-dominated (p→s) and non-dipole (p→p) components, respectively. The latter (p→p) quadrupole component is similar to that observed for the GOS profile of the $7e\rightarrow 11a_1$ (HOMO→LUMO) transition in CF_3Cl, which contains a dominant peak with maximum at $K^2\approx 1.0$ a.u. (Fig. 5) [32]. The GOS profile corresponding to Cl $2p_{3/2}\rightarrow 8e$ and Cl $2p_{3/2}\rightarrow 12a_1$ transitions (Fig. 14c) is found to be noticeably different from that of Cl $2p_{3/2}\rightarrow 11a_1$ (Fig. 14a). In particular, it contains a well-defined secondary peak with a maximum at $K^2\approx 1.6$ a.u. and a notable relative minimum at $K^2\approx 0.8$ a.u. As noted above, the 8e and $12a_1$ orbitals of CF_3Cl contain predominantly σ^*_{C-F} overlaps involving F (s, p) with C (p_x, p_y) and C (s, p_z), respectively. Since the 8e and $12a_1$ orbitals also contain minor Cl (p_x, p_y) and Cl (s, p_z) components respectively, the GOS maxi-

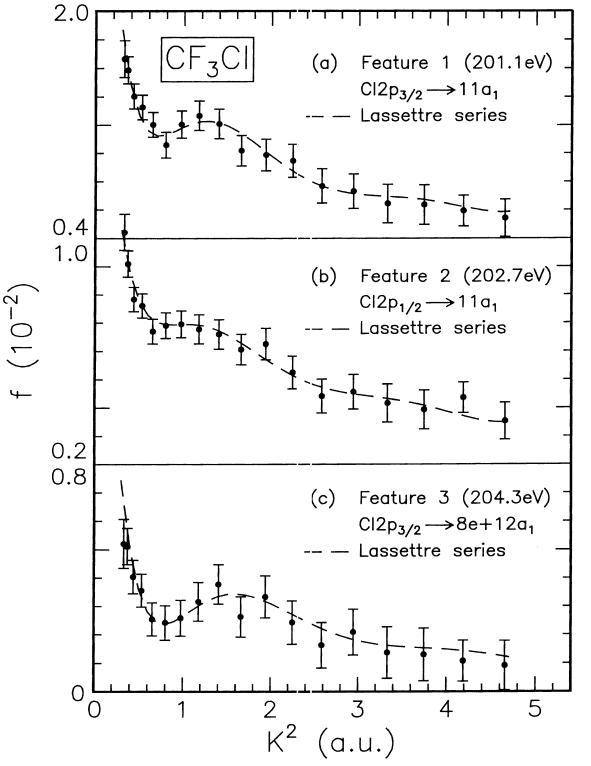

Fig. 14. Absolute generalized oscillator strength (f) as a function of momentum transfer (K) squared for the energy loss features at (a) 201.1 eV, (b) 202.7 eV, and (c) 204.3 eV of CF_3Cl. Plausible predominant assignments for these features as well as semiempirical fits to the respective data using the Lassettre series (dashed lines) are also indicated [35].

mum at $K \approx 0$ corresponds to the p→s type transition for the $12a_1$ final-state orbital while the secondary maximum at $K^2 \approx 1.6$ a.u. may have p→p type contributions from both the $12a_1$ and 8e final-state orbitals. The notable secondary maximum for this particular feature is therefore consistent with additional contribution from the 8e orbital.

The observed trend of increasing dipole component in the GOS profile with successive chlorination for these inner-shell transitions [35] is analogous to that observed for the low-lying $n \rightarrow \sigma^*$ features in the valence shell discussed in Section 4. Clearly, quantitative understanding of this trend must go beyond the present simple consideration of spatial overlaps between the initial-state and final-state orbitals involved. Other phenomena such as the Jahn–Teller effects and core-level relaxation effects that may contribute to the observed dipole components must also be considered. In particular, distortion of degenerate states due to Jahn–Teller effects [64] can introduce additional dipole-allowed transition overlaps. This symmetry breaking mechanism becomes more important in a molecule with higher symmetry such as CCl_4. Furthermore, the increasing size of the atomic constituents in the molecule is generally associated with stronger core-level relaxation, which could also introduce further dipole components. More experimental and theoretical studies are clearly necessary to investigate these fascinating inner-shell effects.

6. Concluding remarks

In summary, we have demonstrated the potential of angle-resolved electron energy loss spectroscopy for electronic structural investigation, especially for the excited state. New low-lying electronic transitions, such as the $n_{Cl} \rightarrow \sigma^*_{C-Cl}$ transitions in the common CFC molecules [32–34] and their HCFC homologs [36–38], have been observed. While this type of transition is both dipole and quadrupole-allowed according to symmetry arguments, their corresponding measured GOS profiles with its maximum oscillator strength at $K^2 \approx 1$ a.u. give convincing evidence that these transitions are predominantly due to quadrupole interaction. Using ab-initio GOS and single-excitation CI excited-state calculations, we show that this type of transition is consistent with an electronic excitation from the non-bonding lone-pair orbital on the Cl atom (HOMO) to an antibonding σ* orbital (LUMO), which leads to dissociation of the C–Cl bond. Control of the momentum transfer (i.e. the scattering angle) may therefore provide a means to observe new metastable or predissociative channels in the electron-induced chemical processes. We have also illustrated that these GOS measurements provide new information about the nature of the multipole excitations in the valence and inner shells of these important cage-like molecules. The study of inner-shell excitations to the excited states (below the ionization continuum) offers new possibilities for further investigating non-dipole excited-state spectroscopy and atom-specific electron-induced chemistry, as well as other fundamental effects such as electron correlation. Together, these GOS data offer a powerful testing ground for ab initio methods for electronic structural calculations for the excited state. Renewed efforts in further improvements of the experimental techniques are now underway at Waterloo. These efforts seek to significantly enhance the signal-to-noise data quality (particularly for inner-shell measurements) through the use of multichannel position-sensitive detection and a high-intensity microfocus electron source, and to develop more quantitative data analysis procedures. Further investigations into the subsequent decay channels following the electron-impact excitation through the use of momentum-transfer-resolved (e,2e) and (e,e+ion) coincidence techniques will also be pursued. These and other continual efforts from other groups will provide the much needed 'absolute' GOS data base and new insights to a fundamental area of electronic spectroscopy that can be distinctly probed by angle-resolved electron scattering techniques.

Acknowledgements

This work was supported by the Natural Sciences and Engineering Research Council of Canada, and in part by NATO and PRF. It would not have been possible without the ingenuity and dedication of Dr. Ji-Feng Ying. We thank Dr. Carl Winstead and Professor Vince McKoy (California Institute of

Technology), Professors Chris Brion (University of British Columbia) and Russ Bonham (Indiana University) for valuable discussions and interactions.

References

[1] J.B. Foresman, M. Head-Gordon, J.A. Pople, M.J. Frisch, J. Phys. Chem. 96 (1992) 135.
[2] H. Bethe, Ann. Phys. 5 (1930) 325.
[3] H. Bethe, Z. Physik 76 (1932) 293.
[4] M. Inokuti, Rev. Mod. Phys. 43 (1971) 297.
[5] R.A. Bonham, J.S. Lee, R. Kennerly, W. St. John, Adv. Quant. Chem. 2 (1978) 1.
[6] E.N. Lassettre, A. Skerbele, in: D. Williams (Ed.), Methods of Experimental Physics, Vol. vol. 3 (Part B), Academic, New York, 1974, p. 868, Chapter 7.2.
[7] E.N. Lassettre, J. Chem. Phys. 43 (1965) 4479.
[8] M.A. Dillon, E.N. Lassettre, J. Chem. Phys. 62 (1975) 2373.
[9] M.A. Dillon, M. Inokuti, Z.W. Wang, Rad. Res. 102 (1985) 151.
[10] A. Hamnett, W. Stoll, G. Branton, C.E. Brion, M.J. van der Wiel, J. Phys. B. 9 (1976) 945.
[11] R.A. Bonham, in: C.R. Brundle, A.D. Baker (Eds.), Electron Spectroscopy: Theory, Techniques and Applications, Vol. vol. 3, Academic, New York, 1979, p. 127.
[12] J.S. Lee, J. Chem. Phys. 67 (1977) 3998.
[13] A. Skerbele, E.N. Lassettre, J. Chem. Phys. 53 (1970) 3806.
[14] J.S. Lee, T.C. Wong, R.A. Bonham, J. Chem. Phys. 63 (1975) 1643.
[15] N. Oda, T. Osawa, J. Phys. B 14 (1981) L563.
[16] G.G.B. de Souza, C.A. Lucas, in: M.J. Coggiola, D.L. Heustis, R.P. Saxon (Eds.), ICPEAC Book of Abstracts, Palo Alto, 1985, North-Holland, Amsterdam, 1985, p. 252.
[17] E. Fainelli, R. Camilloni, G. Petrocelli, G. Stefani, Nuovo Cimento D 9 (1987) 33.
[18] R.S. Barbieri, R.A. Bonham, Phys. Rev. A 45 (1992) 7929, and references therein.
[19] A.C.A. Souza, G.G.B. de Souza, Phys. Rev. A 38 (1988) 4488.
[20] K.N. Klump, E.N. Lassettre, Chem. Phys. Lett. 51 (1977) 99.
[21] K.N. Klump, E.N. Lassettre, J. Chem. Phys. 68 (1978) 3511.
[22] D.A. Shaw, G.C. King, F.H. Read, D. Cvejanovic, J. Phys. B 15 (1982) 1785.
[23] R. Camilloni, E. Fainelli, G. Petrocelli, G. Stefani, J. Phys. B 20 (1987) 1839.
[24] J.T. Francis, N. Kosugi, A.P. Hitchcock, J. Chem. Phys. 101 (1994) 11429.
[25] H.M. Boechat Roberty, C.E. Bielschowsky, G.G.B. de Souza, Phys. Rev. A 44 (1991) 1694.
[26] M.P. de Miranda, C.E. Bielschowsky, H.M. Boechat Roberty, G.G.B. de Souza, Phys. Rev. A 49 (1994) 2399.
[27] J.T. Francis, C. Enkvist, S. Lunell, A.P. Hitchcock, Can. J. Phys. 72 (1994) 879.
[28] J.F. Ying, C.P. Mathers, K.T. Leung, Phys. Rev. A 47 (1993) R5.
[29] J.T. Francis, C.C. Turci, T. Tyliszczak, G.G.B. de Souza, N. Kosugi, A.P. Hitchcock, Phys. Rev. A 52 (1995) 4665.
[30] C.C. Turci, J.T. Francis, T. Tyliszczak, G.G.B. de Souza, A.P. Hitchcock, Phys. Rev. A 52 (1995) 4678.
[31] A.P. Hitchcock, I.G. Eustatiu, J.T. Francis, C.C. Turci, J. Elec. Spec. Relat. Phenom. 88–91 (1998) 77.
[32] J.F. Ying, C.P. Mathers, K.T. Leung, H.P. Pritchard, C. Winstead, V. McKoy, Chem. Phys. Lett. 212 (1993) 289.
[33] J.F. Ying, K.T. Leung, J. Chem. Phys. 101 (1994) 8333.
[34] J.F. Ying, K.T. Leung, J. Chem. Phys. 100 (1994) 7120.
[35] J.F. Ying, K.T. Leung, J. Chem. Phys. 101 (1994) 7311, and references therein.
[36] J.F. Ying, K.T. Leung, J. Chem. Phys. 100 (1994) 1011.
[37] J.F. Ying, K.T. Leung, J. Chem. Phys. 105 (1996) 2188.
[38] J.F. Ying, K.T. Leung, Phys. Rev. A 53 (1996) 1476.
[39] W.M. Huo, J. Chem. Phys. 71 (1979) 1593.
[40] J.F. Ying, T.A. Daniels, C.P. Mathers, H. Zhu, K.T. Leung, J. Chem. Phys. 99 (1993) 3390, and references therein.
[41] L.C. Lee, R.W. Carlson, D.L. Judge, M. Ogawa, J. Quant. Spectrosc. Radiat. Transfer 13 (1973) 1023.
[42] B.E. Cole, R.N. Dexter, J. Phys. B 11 (1978) 1011.
[43] L. de Reilhac, N. Damany, J. Quant. Spectrosc. Radiation Transfer 18 (1977) 121.
[44] W.F. Chan, G. Cooper, R.N.S. Sodhi, C.E. Brion, Chem. Phys. 170 (1993) 81.
[45] A. Szabo, N.S. Ostlund, Chem. Phys. Lett. 17 (1972) 163.
[46] C. Chung, L. Lin, Phys. Rev. A 6 (1972) 998.
[47] E. Bielschowsky, M.A.C. Nascimento, E. Hollauer, Phys. Rev. A 42 (1990) 5223.
[48] R.D. Hudson (Ed.), Chlorofluoromethanes and the Stratosphere, NASA Scientific and Technical Information Office, 1977, NASA Ref. Publication 1010.
[49] Japan Technical Information Services, Plasma Reactions and Their Applications, in: Japan Materials Report, ASM International, 1988.
[50] G.C. King, J.W. McConkey, J. Phys. B 11 (1978) 1861.
[51] W. Zhang, G. Cooper, T. Ibuki, C.E. Brion, Chem. Phys. 151 (1991) 343, and references therein.
[52] R. Gilbert, P. Sauvageau, C. Sandorfy, J. Chem. Phys. 60 (1974) 4820.
[53] J. Doucet, P. Sauvageau, C. Sandorfy, J. Chem. Phys. 58 (1973) 3708.
[54] L.C. Lee, E. Phillips, D.L. Judge, J. Chem. Phys. 67 (1977) 1237.
[55] G.G.B. de Souza, C.E. Bielschowsky, C.A. Lucas, A.C.A. Souza, Phys. Rev. A 42 (1990) 1363, and references therein.
[56] W.A. Goddard III, W.J. Hunt, Chem. Phys. Lett. 3 (1969) 414.
[57] M.J. Frisch, M. Head-Gordon, G.W. Trucks, J.B. Foresman, H.B. Schlegel, K. Raghavachari, M. Robb, J.S. Binkley, C. Gonzalez, D.J. Defrees, D.J. Fox, R.A. Whiteside, R. Seeger, C.F. Melius, J. Baker, R.L. Martin, L.R. Kahn, J.J.P. Stewart, S. Topiol, J.A. Pople, GAUSSIAN 90. Revision F, Gaussian Inc, Pittsburgh, 1990.
[58] M.J. Molina, F.S. Rowland, Rev. Geophys. Space Phys. 13 (1975) 1.
[59] J.L. Dehmer, D. Dill, A.C. Parr, in: S.P. McGlynn, G.L.

Findley, R.H. Huebner (Eds.), Photophysics and Photochemistry in the Vacuum Ultraviolet, Reidel, Dordrecht, 1985, p. 341, and references therein.
[60] J.W. Gallagher, C.E. Brion, J.A.R. Samson, P.W. Langhoff, J. Phys. Chem. Ref. Data 17 (1988) 9.
[61] W. Zhang, T. Ibuki, C.E. Brion, Chem. Phys. 160 (1992) 435, and references therein.
[62] A.P. Hitchcock, D.C. Mancini, J. Elec. Spec. Relat. Phenom. 67 (1994) 1.
[63] C. Winstead, H.P. Pritchard, V. McKoy, private communications, 1993.
[64] J.H.D. Eland, in: Photoelectron Spectroscopy, Butterworth, London, 1974, p. 143.